The Astrophysical Journal Letters, 933:L14 (9pp), 2022 July 1 https://doi.org/10.3847/2041-8213/ac78dd

Divergence in Mass Ratio Distributions between Low-mass and High-mass Coalescing Binary Black Holes

Yin-Jie Li (李银杰)[1,2,3], Yuan-Zhu Wang (王远瞩)[1,3], Shao-Peng Tang (唐少 鹏)[1,2], Qiang Yuan (袁强)[1,2], Yi-Zhong Fan (范一中)[1,2], and Da-Ming Wei (韦大明)[1,2]
[1] Key Laboratory of Dark Matter and Space Astronomy, Purple Mountain Observatory, Chinese Academy of Sciences, Nanjing 210023, People's Republic of China; yzfan@pmo.ac.cn
[2] School of Astronomy and Space Science, University of Science and Technology of China, Hefei, Anhui 230026, People's Republic of China
Received 2022 March 18; revised 2022 June 13; accepted 2022 June 15; published 2022 June 30

Abstract

Coalescing binary black hole (BBH) systems are likely formed via several channels, and it is challenging to understand their formation/evolutionary processes. Some features in the mass function of the primary components (m_1), such as the distinct Gaussian-like peak located at $\sim 34\,M_\odot$, have been previously found. In this work, we investigate the possible dependence of the mass ratio ($q = m_2/m_1$) distribution on the primary mass. We find a Bayesian odds ratio of 18.1 in favor of divergence in the mass ratio distributions between the low- and high-mass ranges over an invariable mass ratio distribution. BBHs with $m_1 \gtrsim 29\ M_\odot$ have a stronger preference of being symmetric compared to those with $m_1 \lesssim 29\,M_\odot$ at a 97.6% credible level. Additionally, we find mild evidence that BBHs with m_1 located in the Gaussian-like peak have a mass ratio distribution different from that of other BBHs. Our findings may favor some formation channels, such as chemically homogeneous evolution and dynamical assembly in globular clusters/nuclear star clusters, which are more likely to provide symmetric BBHs in the high-mass range.

Unified Astronomy Thesaurus concepts: Gravitational wave astronomy (675); High energy astrophysics (739)

1. Introduction

The first successful detection of a gravitational-wave (GW) signal from a coalescing binary black hole (BBH) on 2015 September 14 (Abbott et al. 2016) has brought about the era of GW astronomy. Very recently, the LIGO–Virgo–KAGRA Collaborations (LVKC) reported the second part of the GW events detected in the third observing run (O3) (The LIGO Scientific Collaboration et al. 2021a), and to date, nearly 100 detections have been reported (Abbott et al. 2019a; The LIGO Scientific Collaboration et al. 2021a; Abbott et al. 2021a; The LIGO Scientific Collaboration et al. 2021b). The number of detections may even reach 1000 once the GW detector network is observing in its design sensitivity (Abbott et al. 2018). However, the origins of these compact objects remain uncertain. Several evolutionary channels have been proposed (see Gerosa & Fishbach 2021; Mapelli 2021 for recent reviews), including, for instance, the isolated binary evolution and dynamical capture. These formation channels will leave an imprint on the properties of the compact binary population (Taylor & Gerosa 2018; Arca Sedda & Benacquista 2019). Therefore, studying the rapidly increasing population of GW events enables us to investigate how compact binaries form. Various studies that employed some analytical models (e.g., Talbot & Thrane 2017; Abbott et al. 2019b, 2021b; The LIGO Scientific Collaboration et al. 2021c) or some nonparametric approaches (e.g., Li et al. 2021b; Tiwari & Fairhurst 2021; Tiwari 2022) were carried out, and some formation/evolutionary processes of compact binaries are being revealed (e.g., Li et al. 2021a; Wang et al. 2021a, 2021b; Safarzadeh & Wysocki 2021; Kimball et al. 2021; Baxter et al. 2021; Galaudage et al. 2021; Tang et al. 2021; Mapelli et al. 2022).

The mass ratio may also carry some information about the formation and evolution mechanism of BBHs. For instance, Fishbach & Holz (2020) found that the two objects in the merging BBHs are more likely to be of comparable mass rather than randomly paired, consistent with the predictions of some formation channels (Dominik et al. 2015; Marchant et al. 2016; Mandel & de Mink 2016; Amaro-Seoane & Chen 2016; Rodriguez et al. 2016; Mandel & Farmer 2022). In particular, Mandel & de Mink (2016; see also Marchant et al. 2016; de Mink & Mandel 2016) proposed a route toward merging massive BHs, i.e., the chemically homogeneous evolution, such that BBHs that form through it are expected to be most likely equal-mass components because the binary systems were in contact (shared mass) on the main sequence before disengaging during subsequent phases of the chemically homogeneous evolution. The traditional isolated evolution channel, i.e., the common-envelope evolution, is also predicted to produce BBHs with comparable mass components. Anyhow, chemically homogeneous evolution can only produce massive binaries with a total BH mass above $\sim 55\ M_\odot$ (Marchant et al. 2016; Mandel & de Mink 2016), which exceeds the majority of the mass range for the common-envelope evolution, and the preference for equal-mass systems by the common-envelope evolution is less extreme than that by the chemically homogeneous evolution. Additionally, dynamical assembly, such as in globular clusters and nuclear star clusters, may also have a strong preference for symmetric masses (see, e.g., Rodriguez et al. 2016; Banerjee 2017; Antonini et al. 2019; Zevin et al. 2021, and their references), and in such channels, heavier BHs are more likely to merge (see Mandel &

[3] Contributed equally.

Farmer 2022 for a recent review). Therefore, the mass ratio distribution of BHs may be dependent on the primary mass.

In this Letter, we perform a hierarchical Bayesian inference to explore the features of the mass ratio distribution in the BBH populations. The work is organized as follows: In Section 2, we introduce the data and the models used for inference, and in Section 3, we present the results. We make our conclusion and discussion in Section 4.

2. Method

2.1. Selected Events

Our analysis focuses on the GW data of BBHs reported in the Gravitational-wave Transient Catalog 3 (GWTC-3; The LIGO Scientific Collaboration et al. 2021a). To ensure the purity of the samples, we adopt a false-alarm rate (FAR) of $0.25\,\mathrm{yr}^{-1}$ as the threshold to select the events. We exclude GW190814 in the analysis because the low secondary mass ($\sim 2.6\,M_{\odot}$) makes it disconnected from the BBH population (Abbott et al. 2021b; Essick et al. 2022) but potentially connected to the recently identified population of NSBHs (Safarzadeh & Wysocki 2021; Tang et al. 2021). Therefore, we adopt a sample of 62 BBHs based on our criterion of $\mathrm{FAR} < 0.25\,\mathrm{yr}^{-1}$. The posterior samples for each BBH event are adopted from the Gravitational Wave Open Science Center (https://www.gw-openscience.org/eventapi/html/GWTC/). For the (new) events in the GWTC-1 (Abbott et al. 2019a), GWTC-2 (Abbott et al. 2021a), GWTC-2.1 (The LIGO Scientific Collaboration et al. 2021b), and GWTC-3 (The LIGO Scientific Collaboration et al. 2021a), we use the "Overall posterior" samples, the "PublicationSamples" samples, the "PrecessingSpinIMRHM" samples, and the "C01: Mixed" samples, respectively.

2.2. Models

With the updated data from the GWTC-3, the simple PowerLaw Peak model is still acceptable (The LIGO Scientific Collaboration et al. 2021c). Therefore, in our analysis, the distribution of the primary masses is described by

$$\begin{aligned}&\pi(m_1|\alpha, m_{\min}, m_{\max}, \delta_m, \lambda, \mu, \sigma)\\&= ((1-\lambda)\mathcal{P}(m_1|-\alpha, m_{\min}, m_{\max}, \delta_m)\\&\quad + \lambda\mathcal{G}(m_1|\mu, \sigma, m_{\min}, m_{\max})),\end{aligned} \tag{1}$$

where m_1 is the primary mass of the BBHs; $-\alpha$, δ_m, are the power-law spectral index and smoothing scale; λ, μ, and σ are the mixing fraction, mean, and width of the Peak component; and $m_{\min}$ and $m_{\max}$ are the low-mass and high-mass cutoffs. Note that the power-law component $\mathcal{P}$ is normalized after the smoothing treatment on its lower boundary as suggested by Wang et al. (2021b), i.e.,

$$\begin{aligned}&\mathcal{P}(m|-\alpha, m_{\min}, m_{\max}, \delta_m)\\&= A_1 m^{-\alpha} S(m|m_{\min}, \delta_m), \text{ for } m \in (m_{\min}, m_{\max}),\end{aligned} \tag{2}$$

where A_1 is the normalization constant and S is the smoothing function (see Abbott et al. 2021b and The LIGO Scientific Collaboration et al. 2021c for details).

In this work, we also use the Broken Powerlaw (see Abbott et al. 2021b for detail) to model the primary mass distribution for checking purposes,

$$\begin{aligned}&\pi(m_1|\alpha_1, m_{\min}, m_{\max}, \delta_m, b, \alpha_2)\\&\propto\begin{cases} m_1^{-\alpha_1} S(m_1|m_{\min}, \delta_m) & m_{\min} < m_1 < m_{\min} + b(m_{\max} - m_{\min})\\ m_1^{-\alpha_2} S(m_1|m_{\min}, \delta_m) & m_{\min} + b(m_{\max} - m_{\min}) < m_1 < m_{\max}\\ 0 & \text{otherwise.}\end{cases}\end{aligned} \tag{3}$$

where $-\alpha_1$ and $-\alpha_2$ are the power-law slopes in the low- and high-mass ranges, and b is the fraction of the way between $m_{\min}$ and $m_{\max}$ at which the primary mass distribution breaks.

The distribution of the secondary masses $\pi(m_2|m_1, \Lambda_2)$, with respect to m_1, is potentially associated with the pairing function, where Λ_2 is the hyperparameter for the m_2 distribution. A simple description for the m_2 distribution is the power-law model widely adopted in the literature (e.g., Abbott et al. 2021b; The LIGO Scientific Collaboration et al. 2021c),

$$\begin{aligned}\pi(m_2|m_1, \beta, \delta_m) = A_2 m_2^{\beta} S(m_2|m_{\min}, \delta_m), \text{ for } m_2\\ \in (m_{\min}, m_1),\end{aligned} \tag{4}$$

where A_2 is the normalization constant. In this model, the constraint on the power-law slope β of this model is found to be sensitive to whether some highly asymmetric events like GW190412[4] are included in the hierarchical analysis (see Abbott et al. 2020 for details). Therefore in this work, we apply another simple parameterization for m_2 distribution,

$$\begin{aligned}\pi(m_2|m_1, \sigma_q) = A_3 \mathcal{G}(m_2|m_1, m_1\sigma_q) \text{ for } m_2\\ \in (m_{\min}, m_1),\end{aligned} \tag{5}$$

i.e., a half-Gaussian with a peak value and width of m_1 and $\sigma_q m_1$, respectively, where A_3 is the normalization constant.

As shown in the posteriors obtained by the default prior (see Figure 1 (a)), many BBHs with primary masses in $\sim(30, 40)\,M_{\odot}$ (i.e., the location of the Peak in the m_1 distribution) show a stronger tendency to have equal masses, though most of the other BBHs are consistent with symmetric systems. When the posteriors are reweighed by a population model with a secondary mass distribution of Equation (5), such a feature becomes more obvious as shown in Figure 1(b). To examine whether and how the mass ratio distribution varies in the whole mass range, we introduce some m_1-dependent mass ratio distribution models. These models take Equation (5) as a prototype, but with σ_q varying with m_1. First, we divide the BBHs into two mass ranges ($m_1 < m_{\mathrm{cut}}$ and $m_1 > m_{\mathrm{cut}}$), where the BBHs have two different mass ratio distributions, hereafter Model I,

$$\sigma_q(m_1|\sigma_q^{\mathrm{low}}, \sigma_q^{\mathrm{high}}, m_{\mathrm{cut}}) = \begin{cases}\sigma_q^{\mathrm{low}} & m_1 < m_{\mathrm{cut}},\\ \sigma_q^{\mathrm{high}} & m_1 > m_{\mathrm{cut}}.\end{cases} \tag{6}$$

To further check how the mass ratio distribution varies with the primary mass in detail, we use the cubic spline to interpolate the $\sigma_q(x)$ that describes the mass ratio distribution of BBHs with $m_1 = x$; such a nonparametric method was initially used to characterize the primary mass function by Edelman et al.

[4] Note that GW190412 is not an outlier because the posterior of β inferred from the inclusion of GW190412 has a significant overlap with the leave-one-out posterior (see Abbott et al. 2021b for details).

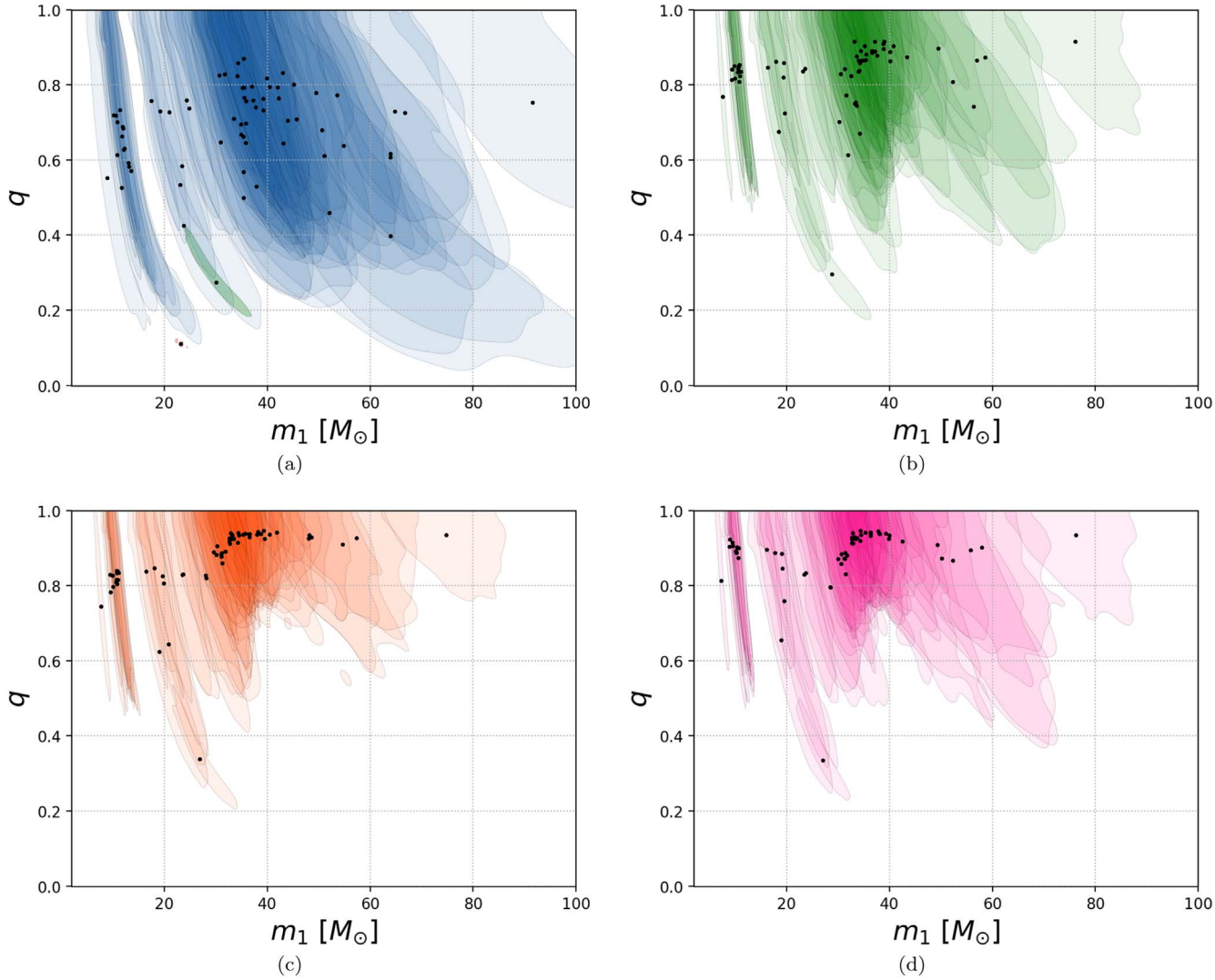

Figure 1. (a) Primary mass and mass ratio posteriors for the 63 BBH candidates (including GW190814) in the LVKC GWTC-3 catalog (The LIGO Scientific Collaboration et al. 2021a) with FARs below 0.25 yr^{-1}, as obtained under a default prior. Each shaded region (black point) represents the central 90% credible posterior bounds (median m_1 and median q value) of a given BBH. The red and green regions represent the three asymmetric systems GW190814 and GW190412. (b) The same as (a), but the posterior samples are reweighted by the POWERLAW PEAK with the half-Gaussian mass ratio model (Equation (2)) described in Section 2.2. (c) The same as (a), but the posterior samples are reweighed by POWERLAW PEAK with the m_1-dependent mass ratio model of Equation (6) described in Section 2.2. (d) The same as (a), but the posterior samples are reweighted by the POWERLAW PEAK with the m_1-dependent mass ratio model of Equation (7) described in Section 2.2.

(2022). So, the corresponding formula is (hereafter Model II),

$$\sigma_{\rm q}(m_1|\sigma_{\rm q}^{\rm left},\sigma_{\rm q}^{\rm right},m_{\rm min},m_{\rm max},\{m_i,f_i\}_{i=1}^{N_{\rm knot}}) = \frac{(m_1-m_{\rm min})\sigma_{\rm q}^{\rm right}+(m_{\rm max}-m_1)\sigma_{\rm q}^{\rm left}}{m_{\rm max}-m_{\rm min}} \times \exp(f(m_1;\{m_i,f_i\}_{i=1}^{N_{\rm knot}})) \quad (7)$$

where $f(m_1;\{m_i,f_i\}_{i=1}^{N_{\rm knot}})$ is the perturbation function modeled as a cubic spline that is interpolated between $N_{\rm knot}$ knots placed in m_1 space, and its shape can be determined by the heights $\{f_i\}$ at their knots $\{m_i\}$. Following Edelman et al. (2022), we fix the locations of each knot to be linear in the log m_1 space of (5, 100) $M_\odot$ and restrict the perturbation to zero at the minimum and maximum knots. We find that 15 knots can make it flexible enough to characterize the mass ratio distribution in the whole primary mass range in detail.

We also try to find out whether the mass ratio distributions are different in the two components of the m_1 distribution (i.e., the POWERLAW and the PEAK). The distributions of the secondary masses in the two components are described by Equation (5) with $\sigma_{\rm q}^{\rm PL}$ and $\sigma_{\rm q}^{\rm G}$. So, Model III reads

$$\pi(m_1|\alpha,m_{\rm min},m_{\rm max},\delta_{\rm m},\lambda,\mu,\sigma,\sigma_{\rm q}^{\rm PL},\sigma_{\rm q}^{\rm G}) = (1-\lambda)\mathcal{P}(m_1|-\alpha,m_{\rm min},m_{\rm max},\delta_{\rm m})\pi(m_2|m_1,\sigma_{\rm q}^{\rm PL}) + \lambda\mathcal{G}(m_1|\mu,\sigma,m_{\rm min},m_{\rm max})\pi(m_2|m_1,\sigma_{\rm q}^{\rm G}). \quad (8)$$

All the parameters, their descriptions, and the priors are summarized in Table 1. Because there is a mass–spin degeneracy, we fit the distribution of primary and secondary masses jointly with the spin distribution and the DEFAULT spin model as defined in The LIGO Scientific Collaboration et al. (2021c) is adopted.

Table 1
Hyperparameters, Their Descriptions, and Chosen Priors for This Work for Each Respective Population Model

Models	Parameters	Descriptions	Priors
		Primary mass distribution models	
PowerLaw Peak	α	slope of the power law	U(−4,12)
	$m_{\rm min}$	minimum mass cutoff	U(2,10)
	$m_{\rm max}$	maximum mass cutoff	U(50,100)
	$\delta_{\rm m}$	width of the mass range that the smoothing function impacts	U(0,10)
	μ	center of the Gaussian component	U(20,50)
	σ	width of the Gaussian component	U(0.5,10)
	λ	fraction of BBH in the Gaussian component	U(0,1)
Broken Powerlaw	α_1	slope of the first power law	U(−4,12)
	α_2	slope of the second power law	U(−4,12)
	$m_{\rm min}$	minimum mass cutoff	U(2,10)
	$m_{\rm max}$	maximum mass cutoff	U(50,100)
	$\delta_{\rm m}$	width of mass range that smoothing function impact on	U(0,10)
	b	fraction between $m_{\rm min}$ and $m_{\rm max}$ where the power-law break lies	U(0,1)
		Mass ratio distribution models	
Half-Gaussian	$\log_{10}\sigma_{\rm q}$	logarithmic width of the mass ratio distribution	U(−2,0)
Model I	$\log_{10}\sigma_{\rm q}^{\rm low}$	$\log_{10}\sigma_{\rm q}$ in the lower-mass range	U(−2,0)
	$\log_{10}\sigma_{\rm q}^{\rm high}$	$\log_{10}\sigma_{\rm q}$ in the higher-mass range	U(−2,0)
	$m_{\rm cut}$	point dividing the lower- and higher-mass ranges	U(20,40)
Model II	$\log_{10}\sigma_{\rm q}^{\rm left}$	$\log_{10}\sigma_{\rm q}$ at the lower-mass edge	U(−2,0)
	$\log_{10}\sigma_{\rm q}^{\rm right}$	$\log_{10}\sigma_{\rm q}$ at the higher-mass edge	U(−2,0)
	$\{f_i\}_{i=1}^{15}$	y-value of the spline interpolant knots	$\mathcal{N}(0,\ \sigma_{\rm knot})$
Model III	$\log_{10}\sigma_{\rm q}^{\rm PL}$	$\log_{10}\sigma_{\rm q}$ in the power-law component	U(−2,0)
	$\log_{10}\sigma_{\rm q}^{\rm G}$	$\log_{10}\sigma_{\rm q}$ in the Gaussian component	U(−2,0)

Note. Here, "U" means the uniform distribution.

2.3. Hierarchical Inference

We perform a hierarchical Bayesian inference to fit the data of the observed events $\{d\}$ with the population models described above. Following the framework described in Abbott et al. (2021b) and The LIGO Scientific Collaboration et al. (2021c), for the given data $\{d\}$ from $N_{\rm det}$ GW detections, the likelihood of the hyperparameters $\mathbf{\Lambda}$ can be expressed as

$$\mathcal{L}(\{d\}|\mathbf{\Lambda}) \propto N^{N_{\rm det}} e^{-N\xi(\mathbf{\Lambda})} \prod_{i=1}^{N_{\rm det}} \int \mathcal{L}(d_i|\theta_i)\pi(\theta_i|\mathbf{\Lambda})d\theta_i, \quad (9)$$

where N is the number of mergers in the universe over the observation period, which is related to the merger rate, and $\xi(\mathbf{\Lambda})$ means the detection fraction. The single-event likelihood $\mathcal{L}(d_i|\theta_i)$ can be estimated using the posterior samples (see Abbott et al. 2021b for detail), and $\xi(\mathbf{\Lambda})$ is estimated using a Monte Carlo integral over detected injections as introduced in the Appendix of Abbott et al. (2021b). We assume that the merger rate density increases with redshift, $\mathcal{R} \propto (1+z)^{2.7}$, as obtained by The LIGO Scientific Collaboration et al. (2021c). The injection campaigns can be adopted from LIGO Scientific Collaboration et al. (2021), where they combine the O1, O2, and O3 injection sets, ensuring a constant rate of injections across the total observing time. We apply the sampler Pymultinest (Buchner 2016) for the hierarchical Bayesian inference of the posteriors.

Table 2
Model Comparison Results

$\ln\mathcal{B}$	m_1 Distribution Models and Events Selection			
Models determining the mass ratio distribution	PLP & full	PLP & leave	BPL & full	BPL & leave
Half Gaussian ($\sigma_{\rm q}$)	0	0	0	0
Model I	2.9	2.5	5.2	5.3
Model II ($\sigma_{\rm knot}=0.5$)	4.0	3.5	3.5	5.0
Model II ($\sigma_{\rm knot}=1$)	4.2	4.1	4.3	5.5
Model III	2.5	1.5	…	…

Notes. Here "PLP" and "BPL" are the abbreviations for PowerLaw Peak and Broken PowerLaw, and "leave" means the case when we leave out GW190412 for analysis. In each case, the values of $\ln\mathcal{B}$ are relative to the evidence of the model with a half-Gaussian mass ratio distribution.

3. Results

In this section, we display the results obtained using the methods described in Section 2. All the results shown here are marginalized over the hyperparameters of the spin distribution. We first compare all the models by the Bayes factors, as summarized in Table 2. Model II provides us with an overall picture[5] of how the mass ratio distribution varies with the

[5] Note that the lower bound of $\sigma_{\rm q}$ in the higher-mass range can still be smaller than that in the range of 30–40 $M_\odot$.

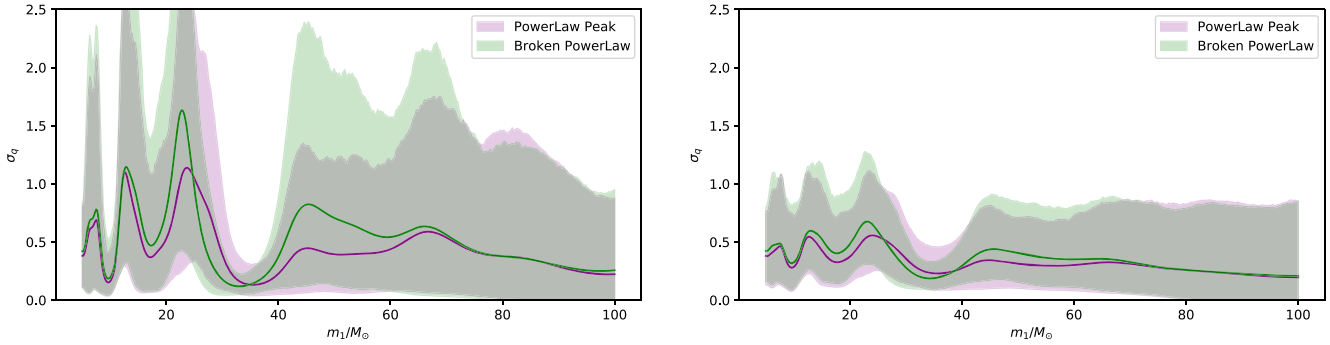

Figure 2. 1σ width of the mass ratio distribution as a function of the primary mass; the shaded regions stand for the 90% credible interval, and the solid curves are the mean values. (a) and (b) are the results obtained using Model II with $\sigma_{\rm knot} = 1.0$ and $\sigma_{\rm knot} = 0.5$.

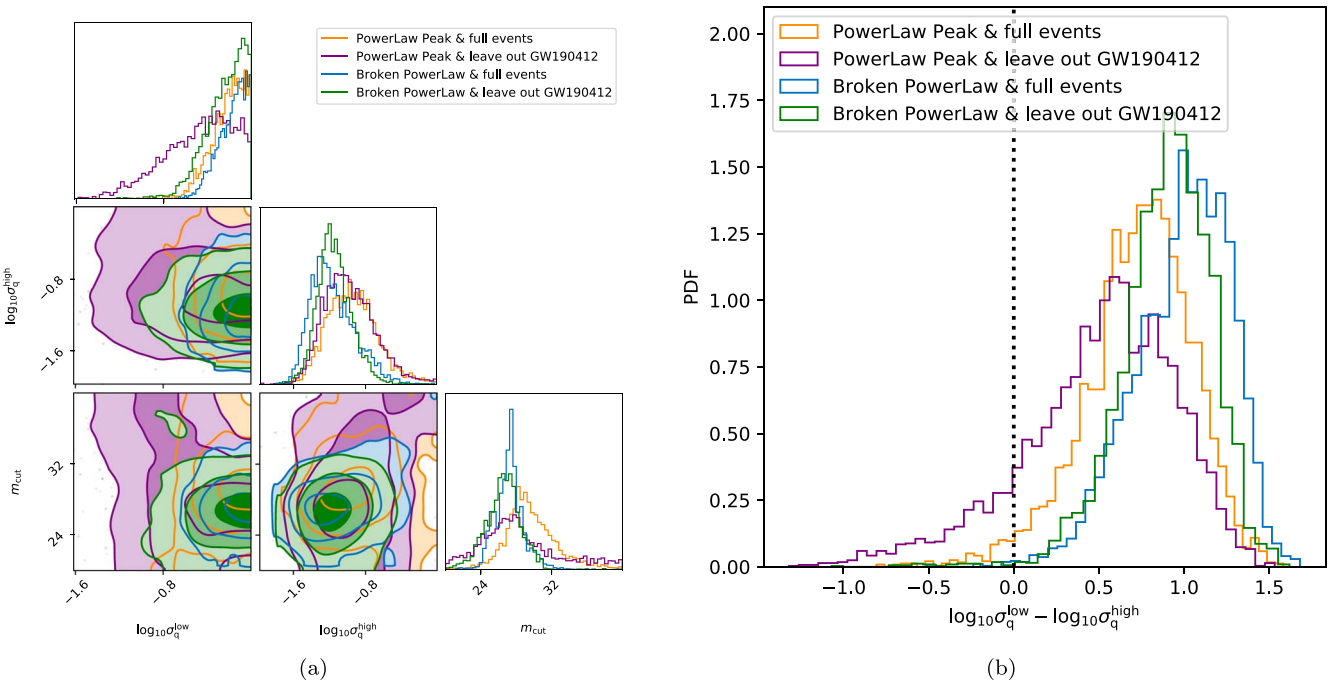

Figure 3. (a) Posterior distributions of $\log_{10}\sigma_{\rm q}^{\rm low}$ ($\log_{10}\sigma_{\rm q}^{\rm high}$) that describe the mass ratio distribution of BBHs in the lower (higher) mass ranges, and the split point $m_{\rm cut}$ obtained by Model I. (b) Posterior distributions of $\log_{10}\sigma_{\rm q}^{\rm low} - \log_{10}\sigma_{\rm q}^{\rm high}$; when we change the primary mass distribution model, the value is still confidently positive, but the credibility becomes lower in the absence of GW190412.

primary mass, as shown in Figure 2. We find nontrivial Bayes factors between Model II (with $\sigma_{\rm knot} = 0.5$ or $\sigma_{\rm knot} = 1$) and the invariable half-Gaussian model. Additionally, the Bayes factors are still significantly positive when we change the primary mass model or exclude the asymmetric event GW190412. So, we conclude that an invariable mass ratio distribution in the whole mass range is disfavored. The mass ratio distribution should vary with primary mass, which indicates that the BBHs in the different mass ranges may have different evolutionary processes.

Model I divides the BBHs into two mass ranges (low and high) at $m_{\rm cut}$, where the mass ratio distributions have two different widths, $\sigma_{\rm q}^{\rm low}$ and $\sigma_{\rm q}^{\rm high}$. We obtained $m_{\rm cut} = 29.3^{+5.7}_{-4.0}\,M_\odot$ (90% credible interval), and the value slightly shifts to a smaller value of $27.4^{+10.2}_{-5.5}\,M_\odot$ if we leave out GW190412 from the analysis. We find that the BBHs in the high-mass range (i.e., with $m_1 > m_{\rm cut}$) have more preference for equal masses than those in the low-mass range (i.e., with $m_1 < m_{\rm cut}$) at a 97.6% credible level, as shown in Figure 3 (a), and the credibility becomes 86.7% in the absence of GW190412. To find out the influence of the primary mass model, we also perform inferences with the BROKEN POWERLAW model (Abbott et al. 2021b) instead of the POWERLAW PEAK (Equation (1)); the conclusion remains unchanged, and the credibility even rises to 99.7%, though $m_{\rm cut}$ slightly shifts to lower values, as shown in Figure 3(b). As shown in Figure 2, $\sigma_{\rm q}$ may wiggle in the lower-mass range ($m_1 < m_{\rm cut}$). To find out whether there are actually additional features, we use an extended Model I (see the Appendix) for analysis. Our results suggest that none of the perturbations are statistically significant enough to declare an additional structure as shown in Figure 6.

The Bayes factors between Model III and the invariable half-Gaussian mass ratio distribution model summarized in Table 2 provide milder evidence that the BBHs with m_1 in the Gaussian component have a mass ratio distribution different from that of the other mass range, as shown in Figure 4 (a). The width of the

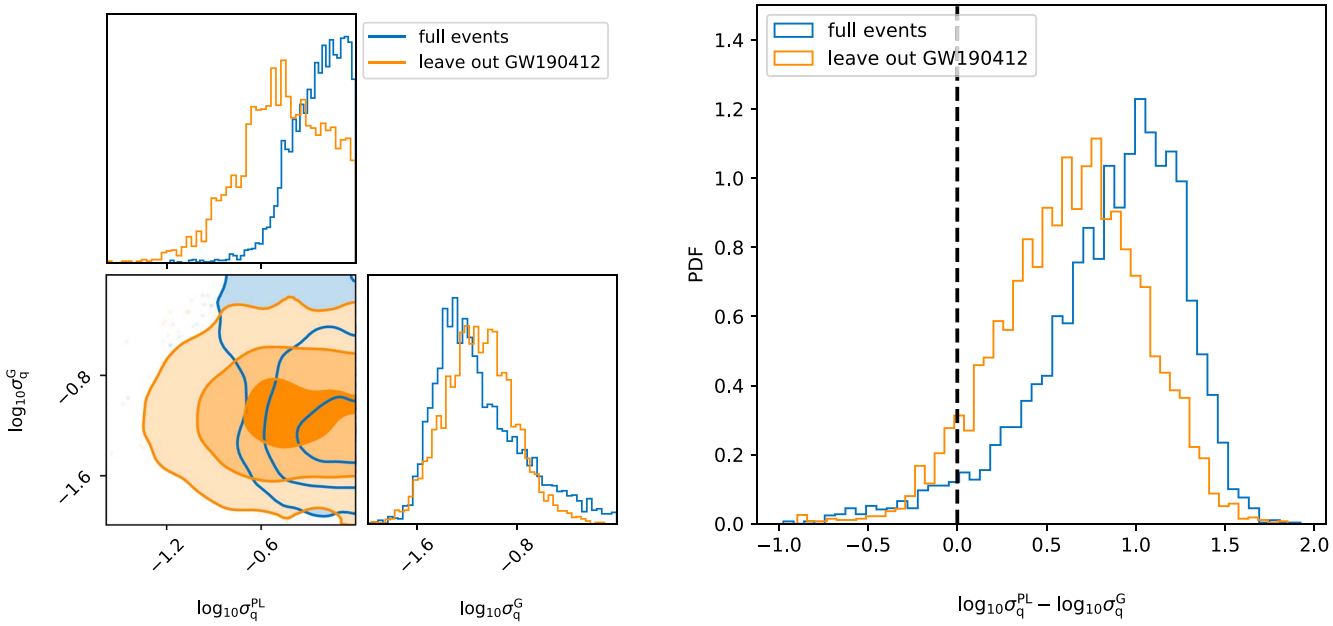

(a) (b)

Figure 4. (a) Posterior distributions of $\log_{10}\sigma_q^{PL}$ ($\log_{10}\sigma_q^G$) that describe the mass ratio distribution of BBHs in the power-law (Gaussian) component obtained by Model III. (b) Posterior distributions of $\log_{10}\sigma_q^{PL} - \log_{10}\sigma_q^G$. When we exclude the GW190412, $\log_{10}\sigma_q^{PL}$ shifts to a smaller value, but the value of $\log_{10}\sigma_q^{PL} - \log_{10}\sigma_q^G$ is still confidently positive.

mass ratio distribution of BBHs in the Gaussian component (σ_q^G) is smaller than that in the power-law component (σ_q^{PL}) at 95.4% credibility (see Figure 4 (b)); such a feature is also present in Figure 2 as well as Figure 1, where the BBHs with $m_1 \sim 35\,M_\odot$ have a stronger preference of being equal-mass systems. When we exclude GW190412 from the analysis, $\sigma_q^{PL} - \sigma_q^G$ is still positive, though σ_q^{PL} shifts to a smaller value. Note that the Gaussian component is almost in the high-mass range for the results obtained by Model II, and we find no evidence that Model III is more preferred than Model I. Therefore, whether the BBHs with primary masses in the Gaussian component have a mass ratio distribution different from the more massive BBHs is inconclusive.

4. Conclusion and Discussion

We have investigated the population of BBHs with some parameterized/semiparameterized models to adequately address some potential features in the mass ratio distribution. With the current coalescing BBH sample (The LIGO Scientific Collaboration et al. 2021a), we first conclude that the mass ratio distribution is not invariable in the whole mass range but varies with the primary mass. This feature may support the fact that the BBHs observed by LIGO/Virgo/KAGRA may come from not only one evolution process. Then, we conclude that BBHs in the higher-mass range are more likely to be equal-mass systems than those in the lower-mass range, and the demarcation point $m_{\rm cut}$ may lie between 25 and 30 $M_\odot$. Consequently, we predict that asymmetric events are more likely to emerge in the lower-mass range. Note that we have excluded GW190814 in our analysis, and our conclusion will be strengthened if we include GW190814, which is potentially located in the lower-mass range. However, from current observations, we cannot conclude yet whether or not there are additional structures in the lower-mass range (see the Appendix for the details of the analysis). In addition to the common-envelope evolution, some formation and evolution channels that have a stronger preference for producing symmetric BBHs, such as chemically homogeneous evolution (Marchant et al. 2016; de Mink & Mandel 2016) and dynamical assembly (Rodriguez et al. 2016; Banerjee 2017; Antonini et al. 2019), have been proposed. BBHs from chemically homogeneous evolution are expected to have total masses above 55 $M_\odot$; meanwhile, for the dynamical assembly in nuclear star clusters, heavier BHs are more likely to merge (Mandel & Farmer 2022). Therefore, our finding that BBHs in the higher-mass range are more likely to be of equal mass is in concert with the predictions resulting from these formation channels.

We also find that BBHs with primary masses in the Gaussian component may have a stronger preference for equal masses than BBHs in the power-law component. This feature in the mass ratio distribution may be associated with pulsational pair-instability supernovae (PPISNe) (Woosley & Heger 2015; Belczynski et al. 2016), because nearly symmetric systems may be built up of the high-mass BHs created from PPISNe. Additionally, as mentioned above, chemically homogeneous evolution and dynamical assembly can also contribute to the nearly symmetric systems in the Gaussian component. However, currently, we find no evidence that BBHs in the Gaussian component are more symmetric than those in the higher-mass range, as described above.

We have qualitatively proven that the mass ratio distribution varies with the primary mass in the surveyed mass range, where the asymmetric systems are more likely to emerge in the lower-mass range, and the BBHs are more symmetric in the higher-mass range. The parameterized/semiparameterized models considered here are still limited and may not be able to describe the BBH populations completely (Mandel & Broekgaarden 2022). For example, it would be beneficial to construct a mass-dependent spin model together with the mass ratio

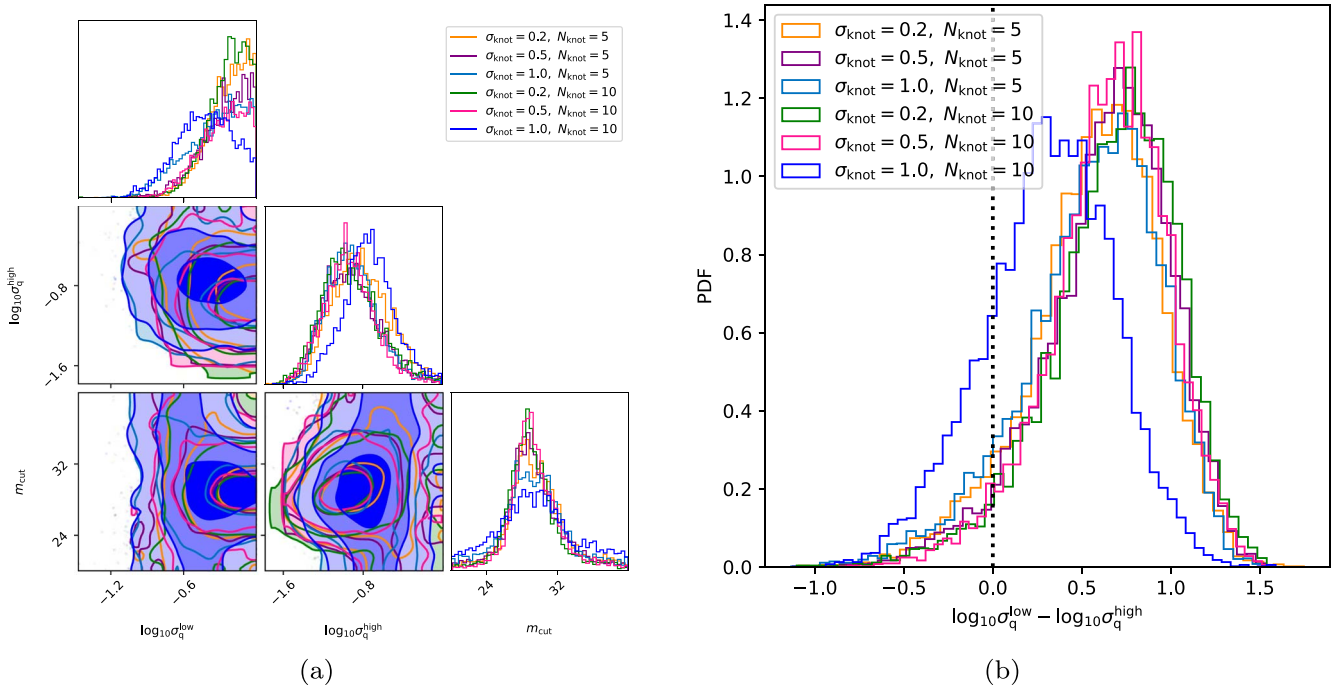

Figure 5. (a) Posterior distributions of $\log_{10}\sigma_{\rm q}^{\rm low}$ ($\log_{10}\sigma_{\rm q}^{\rm high}$) that describe the mass ratio distribution of BBHs in the lower (higher) mass ranges, and the split point $m_{\rm cut}$ obtained by the Extended Model I. (b) Posterior distributions of $\log_{10}\sigma_{\rm q}^{\rm low}-\log_{10}\sigma_{\rm q}^{\rm high}$.

distribution, and we leave this for future work. Meanwhile, the BBH sample is expected to increase rapidly in the near future (Abbott et al. 2018). Therefore, with a significantly extended sample, besides better characterizing the mass ratio distribution in the whole mass range, new structures may be revealed in the mass spectrum and distribution of spin properties of BBHs, shedding new light onto BBH formation channels.

We thank the anonymous referee for constructive suggestions. This work was supported in part by NSFC under grant Nos. 11921003, 11703098, and 12073080; the Chinese Academy of Sciences via the Strategic Priority Research Program (grant No. XDB23040000) and the Key Research Program of Frontier Sciences (No. QYZDJ-SSW-SYS024). This research has made use of data and software obtained from the Gravitational Wave Open Science Center (https://www.gw-openscience.org), a service of LIGO Laboratory, the LIGO Scientific Collaboration and the Virgo Collaboration. LIGO is funded by the US National Science Foundation. Virgo is funded by the French Centre National de Recherche Scientifique (CNRS), the Italian Istituto Nazionale della Fisica Nucleare (INFN) and the Dutch Nikhef, with contributions by Polish and Hungarian institutes.

Software: Bilby (Ashton et al. 2019, version 1.1.4, ascl:1901.011 https://git.ligo.org/lscsoft/bilby/), PyMultiNest (Buchner 2016, version 2.11, ascl:1606.005, https://github.com/JohannesBuchner/PyMultiNest), PyCBC (Biwer et al. 2019; Nitz et al. 2021, gwastro/pycbc: PyCBC Release v1.16.14 https://github.com/gwastro/pycbc).

Appendix
Are There Additional Structures in the Lower-mass Range?

It seems that there are additional structures in the mass ratio distribution in the lower-mass range (i.e., $m_1 < 30\,M_\odot$) as shown in Figure 2. To investigate this range in more detail, we make some modifications to Model I (hereafter Extended Model I),

$$\sigma_{\rm q}(m_1|\sigma_{\rm q}^{\rm low},\sigma_{\rm q}^{\rm high},m_{\rm cut},\{m_i,f_i\}_{i=1}^{N_{\rm knot}}) = \sigma_{\rm q}(m_1|\sigma_{\rm q}^{\rm low},\sigma_{\rm q}^{\rm high},m_{\rm cut})\exp(f(m_1;\{m_i,f_i\}_{i=1}^{N_{\rm knot}})), \quad \text{(A1)}$$

where $\sigma_{\rm q}(m_1|\sigma_{\rm q}^{\rm low},\sigma_{\rm q}^{\rm high},m_{\rm cut})$ is described by Equation (6). We fix the locations of each knot to be linear in log m_1 space of (5, 30) $M_\odot$ and restrict the perturbation to zero at the minimum knot. Here we consider two settings for the number of knots ($N_{\rm knot}=5$ and $N_{\rm knot}=10$), and three values for $\sigma_{\rm knot}$ (0.2, 0.5, 1.0).

First, we find that the values of $\sigma_{\rm q}^{\rm low}$, $\sigma_{\rm q}^{\rm high}$, and $m_{\rm cut}$ obtained in all cases as shown in Figure 5 are consistent with those inferred by Model I as shown in Figure 3. Note that a more flexible perturbation function may allow the $\log_{10}\sigma_{\rm q}^{\rm low}$ to support smaller values, like the case of ($N_{\rm knot}=10$, $\sigma_{\rm knot}=1.0$). To find out whether there are additional structures in the mass ratio distribution in the lower-mass range ($m_1 < m_{\rm cut}$), we plot the perturbation functions, $f(m_1)$, as shown in the upper row of Figure 6. It shows that the three most apparent perturbations lie at $\sim 9\,M_\odot$, $\sim 13\,M_\odot$, and $\sim 25\,M_\odot$. We find $f(m_1=25\,M_\odot)>0$ at 69%, 84%, 78%, and 90% credibility for the settings ($N_{\rm knot}=5$, $\sigma_{\rm knot}=0.5$), ($N_{\rm knot}=5$, $\sigma_{\rm knot}=1.0$), ($N_{\rm knot}=10$, $\sigma_{\rm knot}=0.5$), and ($N_{\rm knot}=10$, $\sigma_{\rm knot}=1.0$), respectively. However, the other two perturbations (i.e., $f(m_1=9\,M_\odot)$ and $f(m_1=13\,M_\odot)$) are much less significant, as shown in the lower row of Figure 6. We find the logarithmic Bayes factors between Extended Model I and Model I for all the cases are $\lesssim 1$. Therefore, we cannot conclude yet that there are additional structures in the mass ratio distribution in the lower-mass range ($m_1 < m_{\rm cut}$).

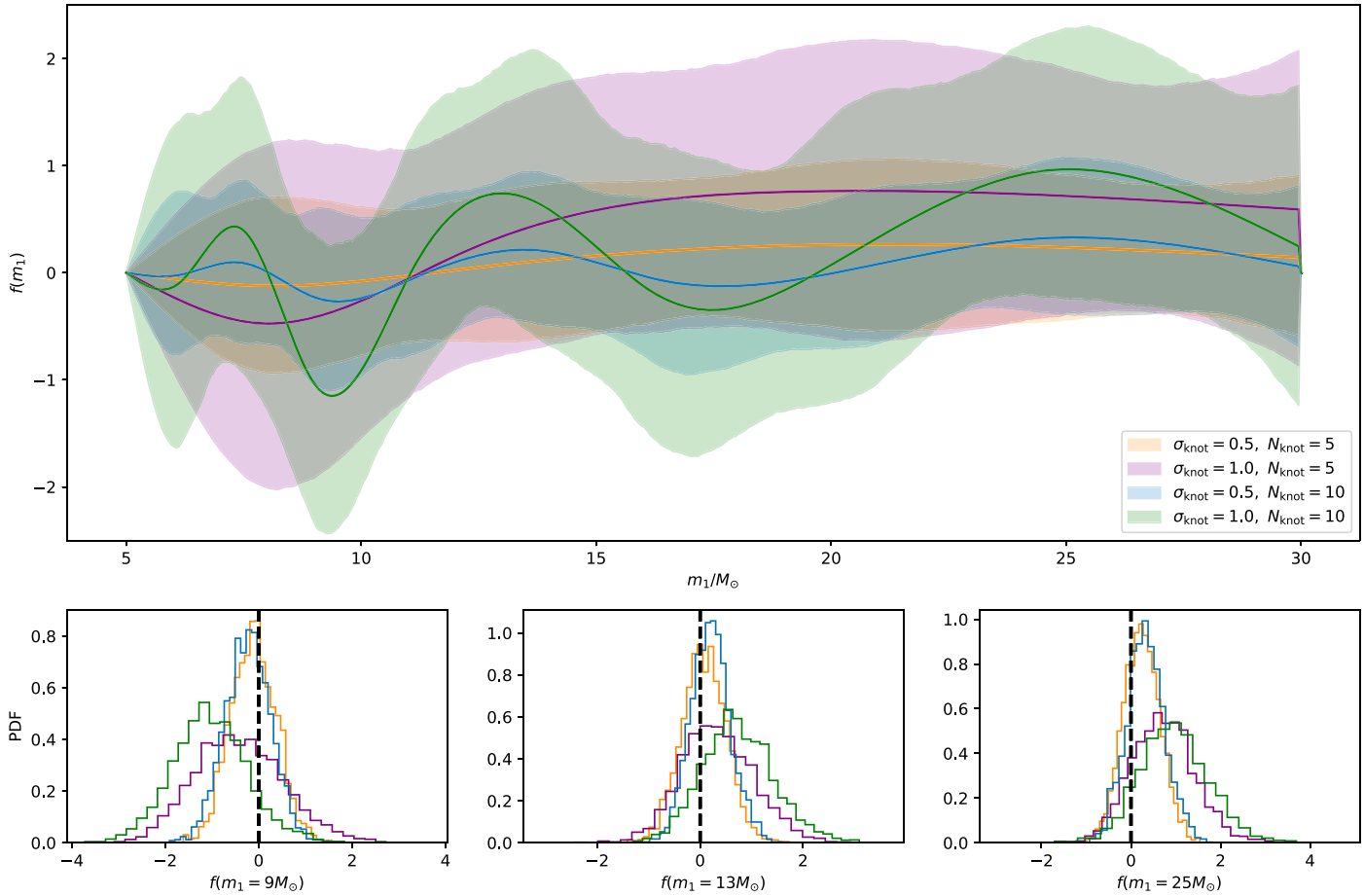

Figure 6. The upper row shows the median (solid) and 90% credible intervals (shaded) of the inferred perturbation functions, $f(m_1)$; the cases for $\sigma_{\rm knot} = 0.2$ are not shown here because the $f(m_1)$ is nearly flat. The lower row shows the posterior distribution of $f(m_1)$ as sliced at the three most apparent inferred perturbations in the posterior, which roughly lie at $\sim 9\ M_\odot$ (left column), $\sim 13\ M_\odot$ (middle column), and $\sim 25\ M_\odot$ (right column).

ORCID iDs

Yin-Jie Li (李银杰) https://orcid.org/0000-0001-5087-9613
Yuan-Zhu Wang (王远瞩) https://orcid.org/0000-0001-9626-9319
Shao-Peng Tang (唐少 鹏) https://orcid.org/0000-0001-9120-7733
Qiang Yuan (袁强) https://orcid.org/0000-0003-4891-3186
Da-Ming Wei (韦大明) https://orcid.org/0000-0002-9758-5476

References

Abbott, B. P., Abbott, R., Abbott, T. D., et al. 2016, PhRvL, 116, 061102
Abbott, B. P., Abbott, R., Abbott, T. D., et al. 2018, LRR, 21, 3
Abbott, B. P., Abbott, R., Abbott, T. D., et al. 2019a, PhRvX, 9, 031040
Abbott, B. P., Abbott, R., Abbott, T. D., et al. 2019b, ApJL, 882, L24
Abbott, R., Abbott, T. D., Abraham, S., et al. 2020, PhRvD, 102, 043015
Abbott, R., Abbott, T. D., Abraham, S., et al. 2021a, PhRvX, 11, 021053
Abbott, R., Abbott, T. D., Abraham, S., et al. 2021b, ApJL, 913, L7
Amaro-Seoane, P., & Chen, X. 2016, MNRAS, 458, 3075
Antonini, F., Gieles, M., & Gualandris, A. 2019, MNRAS, 486, 5008
Arca Sedda, M., & Benacquista, M. 2019, MNRAS, 482, 2991
Ashton, G., Hübner, M., Lasky, P. D., et al. 2019, Bilby: Bayesian inference library, Astrophysics Source Code Library, ascl:1901.011
Banerjee, S. 2017, MNRAS, 467, 524
Baxter, E. J., Croon, D., McDermott, S. D., & Sakstein, J. 2021, ApJL, 916, L16
Belczynski, K., Heger, A., Gladysz, W., et al. 2016, A&A, 594, A97
Biwer, C. M., Capano, C. D., De, S., et al. 2019, PASP, 131, 024503
Buchner, J. 2016, PyMultiNest: Python interface for MultiNest, Astrophysics Source Code Library, ascl:1606.005
LIGO Scientific Collaboration, Virgo Collaboration, and KAGRA Collaboration 2021, GWTC-3: Compact Binary Coalescences Observed by LIGO and Virgo During the Second Part of the Third Observing Run—O3 search sensitivity estimates, Zenodo, doi:10.5281/zenodo.5546676
de Mink, S. E., & Mandel, I. 2016, MNRAS, 460, 3545
Dominik, M., Berti, E., O'Shaughnessy, R., et al. 2015, ApJ, 806, 263
Edelman, B., Doctor, Z., Godfrey, J., & Farr, B. 2022, ApJ, 924, 101
Essick, R., Farah, A., Galaudage, S., et al. 2022, ApJ, 926, 34
Fishbach, M., & Holz, D. E. 2020, ApJL, 891, L27
Galaudage, S., Talbot, C., Nagar, T., et al. 2021, ApJL, 921, L15
Gerosa, D., & Fishbach, M. 2021, NatAs, 5, 749
Kimball, C., Talbot, C., Berry, C. P. L., et al. 2021, ApJL, 915, L35
Li, Y.-J., Tang, S.-P., Wang, Y.-Z., et al. 2021a, ApJ, 923, 97
Li, Y.-J., Wang, Y.-Z., Han, M.-Z., et al. 2021b, ApJ, 917, 33
Mandel, I., & Broekgaarden, F. S. 2022, LRR, 25, 1
Mandel, I., & de Mink, S. E. 2016, MNRAS, 458, 2634
Mandel, I., & Farmer, A. 2022, PhR, 955, 1
Mapelli, M. 2021, in Handbook of Gravitational Wave Astronomy, ed. C. Bambi et al., Vol. 4 (Berlin: Springer), 1
Mapelli, M., Bouffanais, Y., Santoliquido, F., Arca Sedda, M., & Artale, M. C. 2022, MNRAS, 511, 5797
Marchant, P., Langer, N., Podsiadlowski, P., Tauris, T. M., & Moriya, T. J. 2016, A&A, 588, A50
Nitz, A., Harry, I., Brown, D., et al. 2021, gwastro/pycbc: v1.16.14, Zenodo, doi:10.5281/zenodo.5347736
Rodriguez, C. L., Chatterjee, S., & Rasio, F. A. 2016, PhRvD, 93, 084029
Safarzadeh, M., & Wysocki, D. 2021, ApJL, 907, L24
Talbot, C., & Thrane, E. 2017, PhRvD, 96, 023012
Tang, S.-P., Li, Y.-J., Wang, Y.-Z., Fan, Y.-Z., & Wei, D.-M. 2021, ApJ, 922, 3
Taylor, S. R., & Gerosa, D. 2018, PhRvD, 98, 083017

The LIGO Scientific Collaboration, the Virgo Collaboration, Abbott, R., et al. 2021a, arXiv:2108.01045
The LIGO Scientific Collaboration, the Virgo Collaboration, the KAGRA Collaboration, et al. 2021b, arXiv:2111.03606
The LIGO Scientific Collaboration, the Virgo Collaboration, the KAGRA Collaboration, et al. 2021c, arXiv:2111.03634
Tiwari, V. 2022, ApJ, 928, 155
Tiwari, V., & Fairhurst, S. 2021, ApJL, 913, L19
Wang, Y.-Z., Fan, Y.-Z., Tang, S.-P., Qin, Y., & Wei, D.-M. 2021a, arXiv:2110.10838
Wang, Y.-Z., Tang, S.-P., Liang, Y.-F., et al. 2021b, ApJ, 913, 42
Woosley, S. E., & Heger, A. 2015, in Very Massive Stars in the Local Universe, ed. J. S. Vink, Vol. 412 (Berlin: Springer), 199
Zevin, M., Bavera, S. S., Berry, C. P. L., et al. 2021, ApJ, 910, 152